First-principles determination of the dynamical properties of Pb_2MgTeO_6

Razvan Caracas and Xavier Gonze
Université Catholique de Louvain, Unité de Physico-Chimie et de Physique de Matériaux, Place Croix du Sud 1, B-1348 Louvain-la-Neuve, Belgium
(Received 25 May 2004; published 1 February 2005)

We address the incommensurate instability in Pb_2MgTeO_6 from first-principles calculations. For this purpose, we study the phonon dispersion relations for the high-temperature cubic and low-temperature average rhombohedral polymorphs of Pb_2MgTeO_6 and we discuss the instabilities in the different phases. We find an incommensurate instability in the low-temperature rhombohedral phase situated within the (110) plane whose position disagrees with the published interpretation of experimental data. In order to reduce this disagreement, we perform a reinterpretation of the experimental electron diffraction pattern, and also compare experimental and theoretical Raman spectra, with only partial success. We finally determine the interatomic force constants, and compare them with those of other perovskites.

DOI: 10.1103/PhysRevB.71.054101 PACS number(s): 61.44.Fw, 63.20.Dj, 64.70.Rh, 78.30.Hv

I. INTRODUCTION

A large number of materials are known to present incommensurately modulated structures.[1–4] Some of them are metals, with a charge density wave ground state. For insulating systems, mechanisms governing the phase transition have not yet been characterized from first principles. There are a few perovskite insulators presenting such phases and all are rock-salt ordered perovskites: Pb_2CoWO_6,[5] Pb_2CdWO_6,[6] $PbSc_{1/2}Ta_{1/2}O_3$,[7] Pb_2MgNbO_6,[8,9] and Pb_2MgTeO_6 (Refs. 8 and 9) (PMT). PMT presents properties that make it a suitable candidate for a fundamental study of the mechanisms governing the incommensurate (IC) phase transition: a simple and ordered structure, an incommensurability present at 0 K and no lock-in transition to a commensurate state.

The experimental studies[8,9] of PMT show an ordered face-centered-cubic structure at high temperature with the $Fm\bar{3}m$ space group (phase I). This phase transforms to a first incommensurately modulated phase at 194 K with the $R\bar{3}m$ average structure (phase II). Under further cooling, this latter phase transforms at 142 K to a second incommensurate phase with $R\bar{3}$ average structure (phase III). The structures of the high-temperature cubic phase and of the low-temperature incommensurate rhombohedral phase were refined on the basis of the experimental diffraction data.[8,9] The presence of the satellite spots around the main Bragg reflexions[10] is the proof of the existence of the incommensurability. Their position was interpreted[8–10] as a modulation along the rhombohedral (111) directions, with wave vector $\mathbf{q}=(\delta\ \delta\ \delta)$, with δ close to 0.1066. The $Fm\bar{3}m$-IC $R\bar{3}m$ phase transition was observed in calorimetric and dielectric data measurements, but no further refinement of the IC $R\bar{3}m$ phase was reported.

The theoretical characterization of the ground-state properties of PMT from first-principles calculations, using the local density approximation (LDA) of the density functional theory (DFT) has been done previously[11] for the phase I and the average phase III. PMT is a 3 eV LDA gap insulator. The agreement between the theoretical and experimental structures are within the usual LDA precision, with smaller deviations for the cubic than the trigonal phase. The deviations of the Born effective charges from the nominal charges are less than 0.5 for Mg, Pb, and O and less than 1.5 for Te. Only the cubic phase presents instabilities at the Brillouin zone center. In a subsequent study,[12] the lattice dynamical properties of PMT were briefly presented, with a preliminary discussion about the position of the wave vector of the incommensurate modulation.

In the present study we analyze in detail the lattice dynamical properties in the whole Brillouin zone for the phase I and the average phase III. We perform the analysis of the interatomic force constants, and build the phonon dispersion relations. We further analyze the instabilities and the corresponding real-space atomic collective displacements. There are two unstable phonon modes in the cubic structure, the most important one forming tubelike unstable regions along the Γ-X lines. It consists of collective rotations of the TeO_6 octahedra. The second unstable mode is restricted to a small neighborhood around the zone center. Along the Γ-L direction, Pb displacements are added to these rotations. We find by interpolation an instability in the rhombohedral phase that lies in the vicinity of the (110) plane along both the $[\bar{1}10]$ and [100] directions, in disagreement with the interpretation of the experimentalists.[8,9] We give a reinterpretation of the published electron diffraction data that partly supports our calculations, and perform an analysis of the Raman data. We discuss the possible origin of the disagreement between theory and experiment and the different problems raised by both approaches. We will show that the $[\bar{1}10]$ instability is confirmed by direct calculations, but disagrees with the Raman data and the diffraction pattern, while the [100] instability is not confirmed by direct calculation, but agrees well both with the Raman data and the diffraction pattern.

The paper is organized as follows. In Sec. II we give the technical details of the calculations. The phonon dispersion relations are discussed in Sec. III. Section IV presents a reinterpretation of the electron diffraction pattern while a comparison of the theoretical and experimental Raman data is performed in Sec. V. The interatomic force constants analysis is presented in Sec. VI. The paper ends with a final discus-

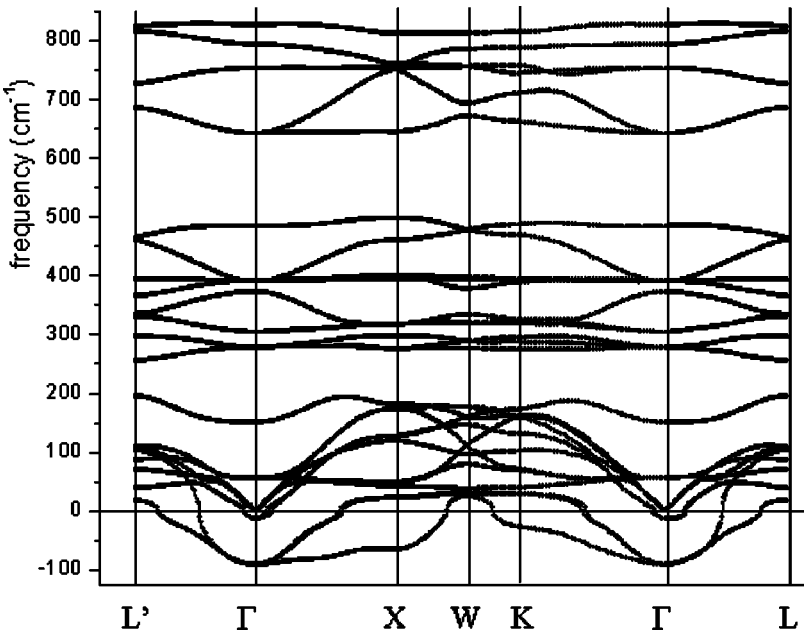

FIG. 1. Phonon bands in the high-temperature cubic phase of Pb_2MgTeO_6.

sion about the different theoretical and experimental problems encountered in our study. In this paper, we adopt the convention that theoretical unstable phonon mode frequencies, whose numerical values are imaginary, will be represented by negative values of the same modulus.

II. COMPUTATIONAL METHODOLOGY

All the calculations are based on the LDA of the DFT,[13,14] as implemented in the ABINIT package [ABINITv2.x, 1999–2000 (Ref. 15) and ABINITv3.x 2001–2002 (Ref. 16)]. The ABINIT software is based on plane waves and pseudopotentials. We use Troullier-Martins pseudopotentials[17] for Mg, Te, and O and an extended Teter norm-conserving pseudopotential[18] for Pb. The considered valence electrons for Pb, Mg, Te, and O are $5d^{10}6s^26p^4$, $3s^2$, $5s^25p^4$, and $2s^22p^4$, respectively. The electronic density and the wave functions used later in the determination of the dynamical matrices are computed on face-centered $2\times2\times2$ special **k** point grids.[19]

The dynamical matrices are calculated on a $4\times4\times4$ grid of special high-symmetry **q** points. These points are defined in the same way as the Monkhorst-Pack special **k** points.[19] The phonon band structures based on interatomic force constants are obtained by Fourier interpolation with specific treatment of the long-range dipole-dipole interaction.[20] For selected low-symmetry **q** wave vectors, we have also performed direct calculations of the dynamical matrices and eigenfrequencies, without interpolation. Technical details on the computation of responses to atomic displacements and homogeneous electric fields can be found in Ref. 20, while Ref. 21 presents the subsequent computation of dynamical matrices, Born effective charges, dielectric permittivity tensors, and interatomic force constants.

All the calculations are performed using the theoretically determined structures. The high-temperature $Fm\bar{3}m$ cubic phase and the low-temperature $R\bar{3}$ average structures are obtained[11] starting from the experimentally reported structures[8,9] and allowing the lattice parameters and the internal coordinates to relax under symmetry constraints. Primitive vectors of theoretical fcc structure are characterized by $a_0=5.539$ Å (with mutual angles $\alpha=60.00°$). The Pb, Mg, Te, and O atoms occupy the $(\frac{1}{4},\frac{1}{4},\frac{1}{4})$, (0,0,0), $(\frac{1}{2},\frac{1}{2},\frac{1}{2})$, and (0.2645,0.2645,0.2645) positions, respectively. The theoretical average rhombohedral phase has $a_0=5.531$ Å and $\alpha=60.27°$. The Pb, Mg, Te, and O atoms occupy, respectively, the (0.2507,0.2507,0.2507), (0,0,0), $(\frac{1}{2},\frac{1}{2},\frac{1}{2})$, and (0.2669,0.2354,0.2949) positions. Thus the rhombohedral distortion of the cubic structure affects mainly the α angle of the primitive cell and the position of the O atoms, and to a lesser extent the lattice parameter and the position of the Pb atoms.

III. PHONON DISPERSION RELATIONS

The phonon dispersion relations for the two analyzed phases are shown in Figs. 1 and 2. The usual conventions for labeling the high symmetry points of the FCC and rhombohedral Brillouin zone are quite different from each other. In Fig. 3, we compare these two notations. As an example, the L point of the fcc Brillouin zone becomes equivalent, in the rhombohedral setting, to two inequivalent points, noted Z (along the trigonal axis) and L. With the fcc Brillouin zone notation, one might refer to these two inequivalent points as L and L'.

The interpolated dispersion curves for the two phases have numerous similarities. We may identify three groups of phonon bands that are separated by relatively large frequency gaps (about 50 and 125 cm^{-1}, respectively, for the first and second gaps). The differences between the phonon bands from the second and third group (in increasing order of energy) for the two structures are very small. The low-frequency modes are instead different, mainly due to the hardening of certain soft modes from the cubic phase during

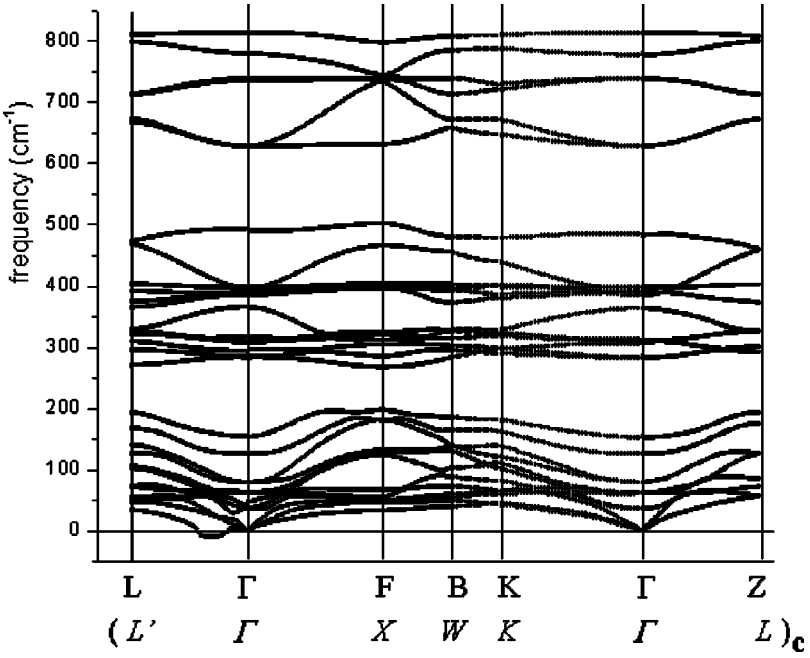

FIG. 2. Phonon bands in the low-temperature average rhombohedral phase of Pb_2MgTeO_6. The high-symmetry points are indexed according to the rhombohedral Brillouin zone, while their cubic equivalent are given between the parentheses on the second line.

the phase transition. The symmetry of the two phases also change the degeneracies of certain bands. The oxygen displacements dominate the eigendisplacements of the modes higher than 250 cm^{-1}, that correspond to breathing modes of the AO_6 octahedra. The cation participation is more important for the modes with a frequency lower than 200 cm^{-1}. We now analyze in more detail, separately, the two phonon band structures.

A. The cubic phase

The cubic phase presents two unstable zone-center phonon modes. The first one, at $91i$ cm^{-1}, has T_{2g} character and is triply degenerated in Γ. Along the Γ-*L* direction it unfolds as 2+1 branches: the twofold degenerated lowest branch stabilizes close to (0.39,0.39,0.39), while the other branch stabilizes closer to Γ at about (0.23,0.23,0.23). Along the Γ-*X* direction it unfolds also as 2+1 branches. The lowest branch does not stabilize along this direction, while the other branches stabilize close to (0.31,0,0).

The three-dimensional image of the most unstable branch of this phonon in the whole reciprocal space is represented in Fig. 4. The instability forms tubelike regions parallel to the Γ-*X* directions. This mode is unstable also in *K* due to the lateral extent of these tubes and to their relative 60° rotation around the [111] directions from the neighboring Brillouin zones. A (001) section through the reciprocal space, where all the three branches of this unstable phonon mode are seen, is shown in Fig. 5. The lowest branch stabilizes along *X*-*W* to become unstable again along *W*-*K*. The other two modes are imaginary in a region around the zone center, that contains also the $\left(\frac{1}{4},0,0\right)$ point.

The eigendisplacements corresponding to this unstable zone-center mode are rotations around the *x*, *y*, or *z* Cartesian axis of the MgO_6 and TeO_6 octahedra. The rotations of these two kinds of octahedra occur in opposite senses. The freezing-in of the rotations corresponding to one of the three modes yields an energetic decrease of 7.014 meV for a 3.2° rotation.

The freezing-in of the octahedral rotations corresponding to all the three modes yields a rhombohedral distortion of the cubic structure. The scalar product between this distortion and the cubic-to-rhombohedral distortion shows a 0.98 overlap.

The lowest branch of the instability from Γ to *X* in the reciprocal space corresponds to the formation of planar

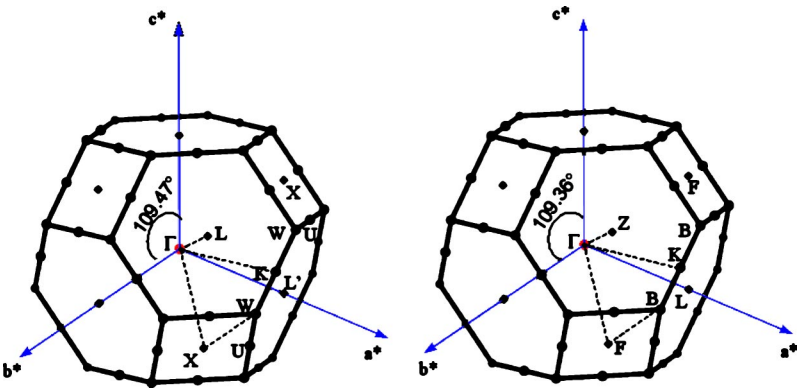

FIG. 3. Brillouin zone for the face-centered-cubic (left) and the rhombohedral (right) lattices. Several high-symmetry points are indicated. The *a**, *b**, and *c** cubic directions correspond to the primitive lattice. In the rhombohedral case, the Γ-*Z* line is along the trigonal axis.

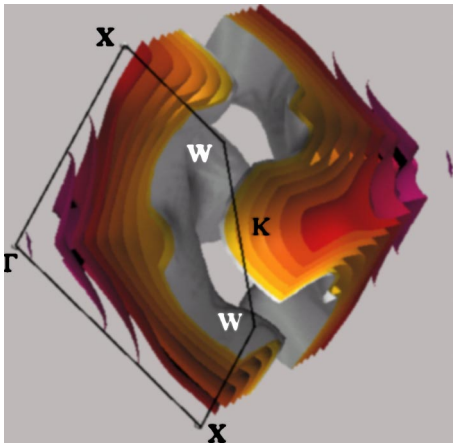

FIG. 4. (Color online) Reciprocal space isofrequency surfaces for unstable phonon modes in the high-temperature cubic phase of Pb_2MgTeO_6. The isofrequency surfaces are spaced by 10 cm^{-1}. The one closest to Γ corresponds to −90 cm^{-1}. There is an inversion symmetry at the center of the figure, and the isosurfaces closest to it corresponds to 0 cm^{-1}.

waves of rotating TeO_6 octahedra. The MgO_6 octahedra are distorted as a result of these rotations and serve as weak coupling links between the TeO_6 octahedra. The different behavior of the TeO_6 and MgO_6 octahedra may be understood from the analysis of the interatomic force constants (Sec. VI).

The second unstable mode is associated with a T_{1u} mode that undergoes a LO-TO splitting. The TO component is weakly unstable, with a $14i$ cm^{-1} frequency, while the LO component is situated at 150 cm^{-1}. This instability is restricted to a very small neighborhood close to Γ. The vibrational pattern for this mode corresponds to parallel displacements of all the atoms in the structure along the *x*, *y*, or *z* Cartesian axis, where the Pb atoms vibrate against all the other atoms of the structure. The differences in the amplitude of atomic displacements are mainly due to the different atomic masses. The largest displacements are recorded for the [*h*00] vibration of the O and Te atoms belonging to the (*h*00) Te+O planes. The Mg and the O atoms situated between these planes have a smaller amplitude of vibration. The displacement of the Pb atoms is the smallest. The freezing-in of the displacements corresponding to only one of the three branches yield an energetic decrease of 0.083 meV for a maximum amplitude of displacement of less than 0.1 Å. The freezing-in of the displacements for the three branches yields a total energetic decrease of 0.105 meV.

B. The average rhombohedral phase

Baldinozzi and co-workers,[8,9] interpreting their experimental data, claimed that the IC structure is characterized by a modulation with a wave vector $\mathbf{q}=(\delta,\delta,\delta)$, along the [111] rhombohedral direction, equivalent to the [111] cubic direction. The measured δ is close to 0.1066 and slightly temperature dependent.

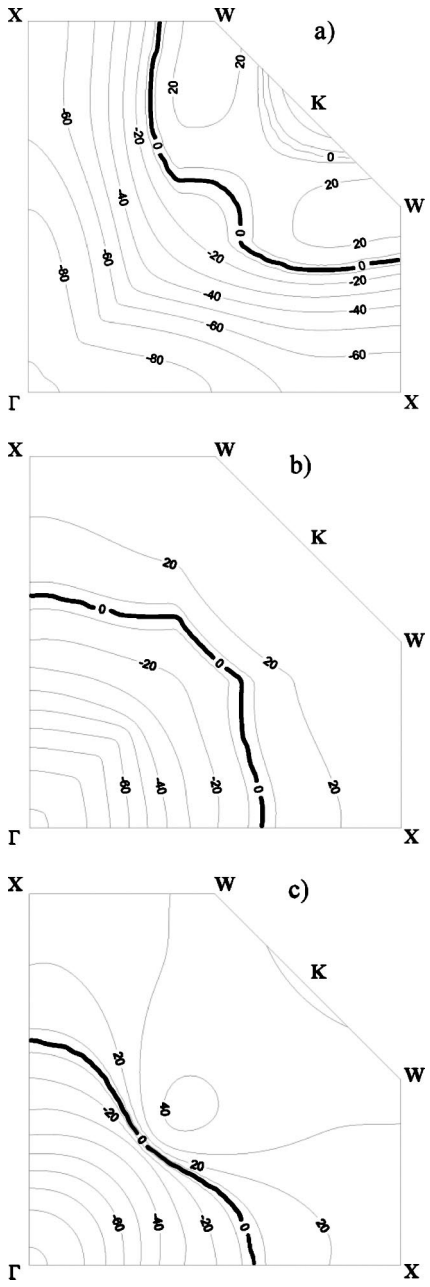

FIG. 5. The isofrequency lines (in cm^{-1}) of the three lowest phonon bands (a), (b), (c) in the high-temperature cubic phase of Pb_2MgTeO_6 viewed in a (001) section through the Brillouin zone.

However, according to our theoretical phonon calculations (Fig. 2) the average rhombohedral phase presents one unstable phonon branch, with the instability situated away from Γ, in the (110) rhombohedral plane, equivalent to the cubic $(1\bar{1}0)$ plane (Fig. 6). The instability is found along both [100] and $[\bar{1}10]$ rhombohedral directions, that are equivalent to the $[\bar{1}11]$ and $[\bar{1}10]$ cubic directions. The minimum of the instability, less than $21i$ cm^{-1}, lies along the $[\bar{1}10]$ rhombohedral direction around the $(\bar{\delta},\delta,0)$ point, with δ close to 0.095. Along the [100] rhombohedral direction the instability lies between (0.0825,0,0) and (0.2125,0,0), with a frequency minimum less than $10i$ cm^{-1} at (0.1525,0,0). The phonon

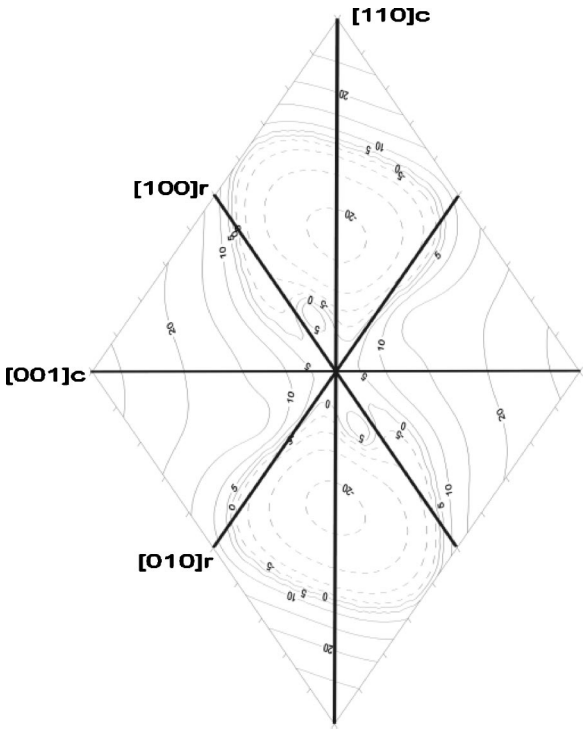

FIG. 6. The unstable phonon mode of the low-temperature average rhombohedral phase of Pb_2MgTeO_6 seen in a rhombohedral (110) section of the reciprocal space. The continuous and dashed isofrequency lines, all separated by 5 cm^{-1}, are for positive and negative frequencies, respectively. The section goes from −0.25 to 0.25 along both [100] and [010] rhombohedral directions. The cubic and rhombohedral directions are indicated, respectively, by the "*c*" and "*r*" indices.

dispersion curves between the [100] and [111] rhombohedral directions, obtained by Fourier interpolation,[20] show a rapid stabilization of the imaginary mode when leaving the [100] line that goes up in frequency towards the [111] line.

Despite our efforts, direct calculations at several **q** points along the [100] rhombohedral direction, using different grids of **k** points (Table I), yield only a slight soft-mode behavior of the lowest phonon that does not confirm the interpolated image and, moreover, is far from the desired convergence. We were not able to reproduce the instability along [100] even using very large grids of **k** points. Instead, direct calculations of the phonon modes at the $\mathbf{q}=(-0.08,0.08,0)$ and $\mathbf{q}=(-0.1,0.1,0)$ rhombohedral points confirm the presence of an unstable mode as obtained by interpolation: the lowest phonon modes lie at $17i$ cm^{-1} and $14i$ cm^{-1}, respectively.

Let us emphasize that the accuracy and convergence requirements placed on these calculations are inherently difficult to reach. Indeed, the square of the phonon frequencies are the eigenvalues of the mass-weighted dynamical matrices. The highest frequencies, around 800 cm^{-1}, are about 100 times larger than the frequencies we are interested in. Taking into account the squaring of frequencies, the typical matrix elements of the dynamical matrix are about 10 000 times larger than the searched eigenvalue.

In any case, our theoretical results disagree with the experimental ones in terms of the direction of the instability: the theoretical instability lies in the vicinity of the (110) rhombohedral plane, which does not contain the [111] rhombohedral direction. We present now a detailed analysis of the available experimental data that somehow decrease the disagreement: the reinterpretation of the published electron diffraction pattern (Sec. IV) and the study of the Raman spectra (Sec. V).

IV. REINTERPRETATION OF THE ELECTRON DIFFRACTION PATTERN

The low-*T* phase of PMT exhibits several sets of satellite spots in the electron diffraction spectra due to the incommensurate modulation. The position of the satellite spots was interpreted in Ref. 10 as $(h+\delta,k+\delta,l+\delta)$, with δ close to 0.1. The authors used the cubic reference system and presented two diffraction images recorded along the cubic $\langle 110\rangle$ directions (Fig. 7).

In the incommensurate phase, with rhombohedral symmetry, the equivalence of the [110] and $[\bar{1}10]$ directions (from the cubic symmetry) is *suppressed* due to the breaking of the symmetry during the transition to the rhombohedral phase. Consequently, the diffraction patterns recorded along [110] and $[\bar{1}10]$ will be different, as clearly seen in Fig. 7. As the distortion of the lattice during the phase transition is expressed in the small change of the rhombohedral angle, which passes from 60.0° to 59.9°, the difference between the two orientations is visible mainly in the disposition of the satellite spots.

TABLE I. Comparison between the Fourier interpolated values and directly obtained values of the frequency of the lowest phonon mode in different points along the rhombohedral [100] direction. The interpolated values (second column) are obtained by Fourier interpolation from a grid of $4\times4\times4$ **q** points. The dynamical matrices are computed using face-centered shifted $2\times2\times2$ grids of special Monkhorst-Pack **k** points. The direct calculations with face-centered shifted $2\times2\times2$ (denoted by $2\times2\times2\times4$), primitive $4\times4\times4$, primitive $8\times4\times4$, and primitive $16\times4\times4$ grids of **k** points are shown in the third, fourth, fifth, and sixth columns, respectively. The vibrational frequencies are expressed in cm^{-1}.

q point	Interpolated value	$2\times2\times2\times4$	$4\times4\times4$	$8\times4\times4$	$16\times4\times4$
(0.0625 0 0)	3	−3	4		18
(0.1250 0 0)	−9	5	5	21	
(0.1875 0 0)	−8		10	24	
(0.2500 0 0)	12	12	18	28	

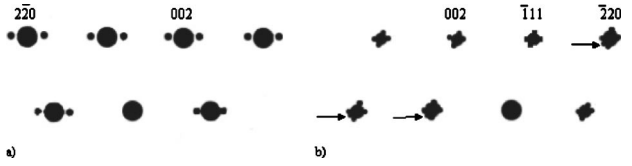

FIG. 7. Schematic representations of the electron diffraction pattern recorded along the [110] (a) and [$\bar{1}$10] (b) cubic directions for the low-temperature cubic phase of Pb_2MgTeO_6 (after Ref. 10). The thin horizontal arrows show the position of the satellite peaks corresponding to the [$\bar{1}$10] direction. All the other satellites correspond to the [$\bar{1}$11] cubic direction (equivalent to [100] rhombohedral). See text for details.

The published interpretation of the spectra claims the position of these satellite spots to be (δ,δ,δ). However, according to the rhombohedral symmetry this will generate two equivalent (δ,δ,δ) and $(\bar{\delta},\bar{\delta},\bar{\delta})$ spots. These spots should be visible only in the [$\bar{1}$10] recorded spectra, while the [110] recorded spectra should present no satellite spots. Obviously, this is in disagreement with Fig. 7.

The theoretical results concerning the phonon dispersion spectra in the average rhombohedral structure of Pb_2MgTeO_6 indicates an incommensurate instability situated in the (110) rhombohedral plane, along both the rhombohedral [100] and [$\bar{1}$10] directions, corresponding to the family of cubic [$\bar{1}$11] and [$\bar{1}$10] directions.

Let us examine the possibility of an incommensurate wave vector along the rhombohedral [100] direction first. Such an incommensurate instability, once frozen in the structure, may be expressed in a diffraction pattern as satellite spots at general positions $(\delta,0,0)$. The rhombohedral symmetry ensures a multiplicity of 6 for these spots. The electron diffraction spectra recorded along the [$\bar{1}$10] direction (according to the cubic reference system) will detect the presence of two satellite spots around the main Bragg spots, with a geometry similar to the one described in Fig. 7(a). The spectra recorded along the perpendicular [110] direction (according to the cubic reference system) will detect the presence of four satellite peaks around the main Bragg spots, with a geometry similar to the one described in Fig. 7(b).

Thus, the theoretical instability situated along the [100] rhombohedral direction is in better agreement with the experimental electron diffraction pattern than the one postulated in Refs. 8 and 9. An independent reindexation of the published experimental electron diffraction pattern confirmed our criticism of the previous interpretation.[22]

The other possibility, an incommensurate instability along the [$\bar{1}$10] rhombohedral direction, will generate satellite spots at general $(\bar{\delta},\delta,0)$ positions. These spots will have also a multiplicity of 6, due to the symmetry, and should be all observed in both diffraction patterns [Figs. 7(a) and 7(b)]. These satellite spots are absent in the image recorded along the [$\bar{1}$10] cubic direction [Fig. 7(a)]. The second image shows certain satellite spots that may be assigned to this modulation wave vector [denoted by the thin horizontal arrows in Fig. 7(b)]. However, these spots are not seen around all the main Bragg reflections. Such satellite spots might be second-order satellites due to a [100] rhombohedral incommensurate modulation, or the result of a twinning or some other planar defects of the structure. Thus, although favored in the theoretical phonon band structure analysis, the [$\bar{1}$10] rhombohedral wave vector is not consistent with experiments.

V. RAMAN PEAK POSITION

The analysis of the Raman spectra constitutes the second argument in favor of a modulation wave vector along the rhombohedral [100] direction.

A. Cubic phase

There are five Raman active modes in the cubic phase of PMT: $2T_{2g}+1T_{1g}+1E_g+1A_{1g}$. In the experimental spectra[8] the T_{1g} mode, stabilized by the temperature, is superposed with one T_{2g} mode, while in the theoretical calculation (at 0 K) the T_{1g} is an imaginary mode, all the other theoretical modes being positive. The experimental (theoretical) T_{2g}, T_{2g}, E_g, A_{1g} modes are situated at 58 (56), 357 (390), 568 (641), 759 (826) cm^{-1}. The deviation of the theoretical results with respect to the experimental ones increase from -2 cm^{-1} for the low-frequency T_{2g} mode to +67 cm^{-1} for the high-frequency A_{1g} mode. The theoretical modes overestimate the experimental data in the high-frequency region by a roughly constant scaling factor (1.1089). Both the theoretical and the experimental data agree on the interpretation of the vibrational pattern and the character assignment of the Raman peaks.

B. Rhombohedral phase

The rhombohedral phase presents a much more complex Raman spectrum, characterized by the existence of large broad peaks with numerous shoulders. The number of peaks increases in the low-frequency region of the diagram. The complexity of the Raman diagram is a consequence of the incommensurate character of the modulation that projects the **q**, 2**q**, etc., points of the Brillouin zone of the average structure to the new zone-center Γ point of the incommensurate phase. Due to the dispersion of the phonon frequencies, the position of the projected modes from **q**, 2**q**, etc., is shifted with respect to the one of the corresponding modes in Γ. This leads to the apparition of the "shoulder" peaks (from $\mathbf{n}\cdot\mathbf{q}$) around the "central" ones (from Γ).

Consequently, we may add to the Raman-active g modes in Γ their correspondents from the modulation wave vector **q** point, and obtain Raman lines whose position are comparable to the measured ones. The different choices of the modulation wave vector, namely, $\mathbf{q}=(\delta\ 0\ 0)$, $\mathbf{q}=(\bar{\delta}\ \delta\ 0)$, or $\mathbf{q}=(\delta\ \delta\ \delta)$ show similar Raman spectra above 50 cm^{-1}. Figure 8 shows the theoretical Raman lines obtained from the folding of the modes in $(\delta,0,0)$ and $(2\delta,0,0)$ on the modes in Γ. The trend of shifting upwards the theoretical modes at high frequencies is observed also in the rhombohedral phase, and the linear correction obtained from the cubic phase may

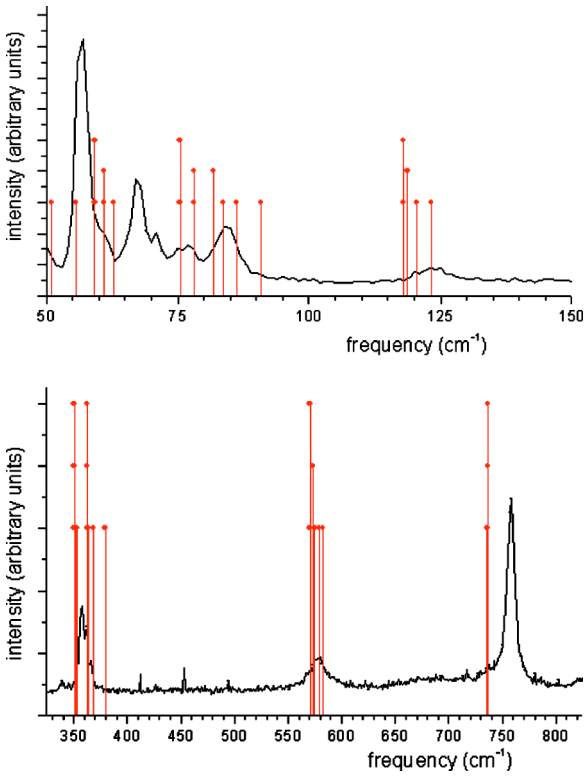

FIG. 8. (Color online) Comparison between the theoretical Raman lines and the experimental spectra, above 50 cm^{-1}. The theoretical lines are obtained from the Raman modes in Γ (highest vertical lines) and the folding of their correspondents in $(\delta,0,0)$ (midhigh vertical lines) and $(2\delta,0,0)$, $(\delta,\delta,0)$, and $(\delta,\bar{\delta},0)$ (lowest vertical lines).

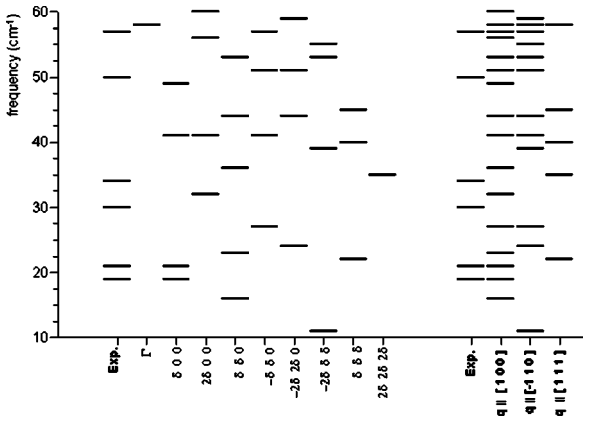

FIG. 9. Comparison between experimental (left column) and theoretical low-frequency Raman lines position for the low-temperature phase of Pb_2MgTeO_6 below 60 cm^{-1}. Γ and different **q** points are represented first independently, then regrouped as a function of the modulation wave vector position: along [100], [$\bar{1}$10], and [111] rhombohedral directions. Many theoretical lines might have weak intensities, so that they would not appear in the experimental spectrum. By contrast, the peaks seen experimentally should be attributed to some existing nearby theoretical line.

be applied. There is a good correspondence between the experimental Raman and the theoretical *g* modes based on the value of the frequency. The only exception is the experimental mode recorded at 152.3 cm^{-1} which is very low in intensity. It may correspond to a *u* mode in **q**, that could be activated as a result of the folding.

The main difference between the modulation wave vector in $\mathbf{q}=(0.1066,0,0)$, according to the theoretical instability obtained by interpolation or by the reinterpretation of the electron diffraction pattern, instead of $\mathbf{q}=(0.1066, 0.1066, 0.1066)$, according to the experimental data, or $\mathbf{q}=(-0.1066, 0.1066, 0)$, according to the lowest unstable mode obtained theoretically, consists of the behavior at low frequency. Figure 9 shows the correspondents of the Raman modes from Γ in the different possible **q** and 2**q** points. The whole theoretical spectrum for the three choices of the modulation wave vector is then obtained from the folding of the corresponding points to Γ.

Theoretically, if we consider the modulation along the [111] direction, due to the high symmetry of all the points along this line, the degeneracy of the phonon modes is large and the number of "shoulder" peaks is quite small: we cannot assign several experimental peaks in the 10–100 cm^{-1} frequency range (Fig. 9). Moreover, the asymmetry of the experimental peaks (such as the 19–21 cm^{-1} one) cannot be obtained. If we consider the modulation along the [$\bar{1}$10] direction, then the experimental peaks at 19 and 21 cm^{-1} are shifted at 24 and 27 cm^{-1}, the experimental peak at 30 cm^{-1} does not have a theoretical correspondent. At last, if we consider the modulation along the [100] direction, then we obtain a reasonable agreement between the experimental and the theoretical modes at 19 and 21 cm^{-1}. The different experimental peaks situated at the 30–60 cm^{-1} have theoretical correspondents within a 5 cm^{-1} range. The large number of theoretical lines comes from the different possible 2**q** points. Their varying intensity may contribute mainly to the broadening seen for the experimental peaks. Consequently the best fit between experiment and theory is obtained by considering the modulation along the [100] direction. This choice ensures a reasonable agreement between the experimental and theoretical modes in terms of both position and mode degeneracy. Due to the low symmetry of the points along this direction, there are no degenerate phonon modes and this may account for the asymmetry of the experimental peaks.

VI. INTERATOMIC FORCE CONSTANTS

The analysis of the interatomic force constants in the two structures can shed some light on the chemical bonding in PMT and the similarities and differences with other perovskite crystals. We analyze first the self-force constants (SFC's), listed in Table II, and then the interatomic force constants (IFC's) between nearest-neighbor atoms, listed in Table III. The SFC is the force acting on an isolated atom during its displacement along a Cartesian direction, all the other atoms in the lattice being fixed.

In the cubic phase, all the SFC are positive, showing that the structure is stable against isolated atomic displacements. The biggest SFC is on the Te atoms, due to the strong bonds with the neighboring O atoms. The only possible way to reduce the energy of the structure is the collective displace-

TABLE II. Self-force constants in the cubic ($Fm\bar{3}m$) and average rhombohedral ($R\bar{3}$) phases of Pb_2MgTeO_6. The values listed for the atoms in the cubic phase and for the Pb, Mg, and Te atoms in the average rhombohedral phase are the diagonal values of the 3×3 tensors (the off-diagonal values vanish for symmetry reasons). For the O atoms in the rhombohedral phase, the 3×3 matrix represents self-force constants along the Cartesian directions. All the values are expressed in Ha/bohr^2.

Atom			
	$Fm\bar{3}m$		
Pb	0.0464	0.0464	0.0464
Mg	0.1094	0.1094	0.1094
Te	0.5278	0.5278	0.5278
O[a]	0.3172	0.0600	0.0600
	$R\bar{3}$		
Pb	0.0552	0.0552	0.0492
Mg	0.1049	0.1049	0.1022
Te	0.5186	0.5186	0.5213
O[b] x	0.2216	−0.0091	−0.1152
y	−0.0091	0.0674	0.0063
z	−0.1152	0.0063	0.1414

[a]The values correspond to the O atom situated along the x Cartesian axis.

[b]The values correspond to the O atom situated at (0.2667, 0.7646 0.7052).

ment of atoms, corresponding to phonon modes. In the rhombohedral phase the SFC are positive for the cations, with values very close to those of the cubic structure. The O atoms have SFC with diagonal positive values and off-diagonal positive and negative values. The eigenvalues are all positive [0.3040 0.0669 0.0595], with one large component and two smaller ones, corresponding to longitudinal or transverse displacements with respect to the direction of the nearest neighbor.

TABLE III. Interatomic force constants (IFC's) in the cubic ($Fm\bar{3}m$) and average rhombohedral ($R\bar{3}$) phases of Pb_2MgTeO_6. The listed values correspond to the eigenvalues of the interatomic force constant tensors, for the nearest-neighbor pairs. The largest eigenvalues (first column) are associated with mostly longitudinal IFC's, the others are mostly associated with transverse IFC's. All the values are expressed in Ha/bohr^2.

Atom pair			
	$Fm\bar{3}m$		
Pb-O	−0.0108	−0.0065	0.0091
Mg-O	−0.0324	−0.0039	−0.0039
Te-O	−0.1733	−0.0371	−0.0371
	$R\bar{3}$		
Pb-O	−0.0116	−0.0066	−0.0003
Mg-O	−0.0290	−0.0042	−0.0042
Te-O	−0.1673	−0.0372	−0.0372

The IFC in the two structures are similar, with differences less than 10%. The IFC for the rhombohedral structure are smaller than those for the cubic one. The Te-O IFC are the strongest, much stronger than the Mg-O IFC's. In the cubic structure, the longitudinal component of the Te-O IFC (parallel with the bond direction) is about six times larger (−0.1733 Ha/bohr^2) than the Mg-O correspondent one (−0.0324 Ha/bohr^2). This difference is responsible for the different behaviors of the TeO_6 and MgO_6 octahedra. The Mg-O weaker bonds act as couplings between the more rigid TeO_6 octahedra. The longitudinal Pb-O IFC's (−0.0108 Ha/bohr^2) are even smaller than Mg-O ones. Consequently, the Pb only weakly influences the phase transition energetics. In the average rhombohedral structure, the same relationships between the IFC's are preserved as for the cubic structure.

The comparison between the cubic structure of PMT with other, simple cubic perovskites[23] ($BaTiO_3$, $PbTiO_3$, and $PbZrO_3$), reveals SFC in PMT stronger than those in $PbTiO_3$ and smaller than those in $BaTiO_3$. The SFC on Mg are smaller than those on Ti (0.139 Ha/bohr^2) in $PbTiO_3$, while those on Te are much stronger. The image of the cation-anion IFC's is different with respect to the other perovskites. Except for the Pb-O longitudinal IFC, all the others are negative in PMT, while positive and negative in the other cases. The Te-O IFC's are the strongest ones, while the Mg-O IFC's are comparable, in absolute value, with the B-O IFC's in the other ABO_3 perovskites.

VII. CONCLUSIONS

We study from first principles the dynamical properties of the cubic high-temperature and the average rhombohedral low-temperature phases of Pb_2MgTeO_6, a rock-salt ordered perovskite that presents an incommensurate displacive modulation at low temperatures. We analyze the phonon dispersion bands and discuss the instabilities in both phases (Sec. III). We perform a reinterpretation of the electron diffraction pattern (Sec. IV) and compare the experimental and theoretical Raman spectra (Sec. V). We finally discuss the interatomic force constants (Sec. VI).

The phonon dispersion bands show two unstable modes in the cubic phase in the zone center. The first one stabilizes very fast out of Γ and the second one persists away from Γ, forming tubelike unstable regions parallel to the Γ-X directions. The instability is found again in K. The atomic displacement pattern corresponding to this instability consists of planes of rotating TeO_6 octahedra.

The phonon bands corresponding to the average rhombohedral structure of the incommensurately modulated phase show the existence of one unstable phonon mode situated in the (110) plane. The instability is found along both the [100] and the $[\bar{1}10]$ directions, the minimum lying along the latter one. This disposition of the instability disagrees with the previously published experimental interpretation which, on the basis of an electron diffraction pattern, claimed a modulation wave vector along the [111] direction, in the $\mathbf{q}=(\delta,\delta,\delta)$ point, with δ close to 0.1066.

In order to argue in favor of the theoretical image obtained after the determination of the phonon dispersion, we performed a careful analysis of the published experimental positions of the satellite peaks that are due to the modulation: the wave vector must be positioned along the [100] rhombohedral direction instead.

The interpretation of the numerous shoulder peaks observed in the Raman diagram recorded for the incommensurate phase shows also a better agreement in folding to the new zone center of the incommensurate phase the corresponding g modes in the $(\delta,0,0)$ rather than the (δ,δ,δ) or $(\bar{\delta},\delta,0)$ **q** points (with $\delta=0.1066$).

However, it appears that both the experimental and theoretical results are still questionable at least with respect to the position of the modulation wave vector: the position of the interpolated instability along the [100] direction, which offers a better agreement with the experimental diffraction, and the Raman data are not confirmed by first-principles direct calculations. The minimum along the $[\bar{1}10]$ direction that was predicted by calculations is not compatible with the disposition and the symmetry of the satellite peaks as shown on the experimental diffraction patterns.

We do not have enough evidence to clearly confirm a condensation of a soft mode as the mechanism of the incommensurate phase transition. An alternate model involving planar defects has been proposed recently for Pb_2ScNbO_6 in Ref. 24, but the presence of solid solutions in this latter material makes a comparison between the two compounds rather useless. The absence of theoretical calculations for other incommensurate perovskites renders our task even more difficult. It is obvious today that further investigations are needed in order to clarify the physics of the incommensurate transitions in rock-salt ordered perovskites.

ACKNOWLEDGMENTS

R.C. acknowledges help from computer scientists B. van Renterghem and J.-M. Beuken. Many thanks go also to G. Baldinozzi, J. Hadermann, K. Rabe, and Ph. Ghosez for fruitful discussions. X.G. acknowledges financial support from the National Fund for Scientific Research (Belgium). Support also came from the FRFC Project No. 2.4556.99 "Simulation numérique et traitement des données."

[1] J. D. Axe, M. Iizumi, and G. Shirane, in *Incommensurate Phases in Dielectrics*, edited by R. Blinc and A. P. Levanyuk (North-Holland, Amsterdam, 1986), pp. 1–48.
[2] H. Z. Cummins, Phys. Rep. **185**, 211 (1990).
[3] Y. Ishibashi, in *Incommensurate Phases in Dielectrics 2*, edited by R. Blinc and A. P. Levanyuk (Elsevier Science Publishers B. V., Amsterdam, 1986), pp. 49–69.
[4] R. Caracas, J. Appl. Crystallogr. **35**, 120 (2002); http://www.mapr.ucl.ac.be/~crystal/
[5] M. Bonin, W. Paciorek, K. Schenk, and G. Chapuis, Acta Crystallogr., Sect. B: Struct. Sci. **51**, 48 (1995).
[6] G. Baldinozzi, G. Calvarin, Ph. Sciau, D. Grebille, and E. Suard, Acta Crystallogr., Sect. B: Struct. Sci. **55**, 1 (1999).
[7] C. A. Randall, S. A. Markgraf, A. S. Bhalla, and K. Baba-Kishi, Phys. Rev. B **40**, 413 (1989).
[8] G. Baldinozzi, Ph. Sciau, and A. Bulou, J. Phys.: Condens. Matter **9**, 10 531 (1997).
[9] G. Baldinozzi, D. Grebille, Ph. Sciau, J-M. Kiat, J. Moret, and J.-F. Berar, J. Phys.: Condens. Matter **10**, 6461 (1998).
[10] G. Baldinozzi, Ph. Sciau, J. Moret, and P. A. Buffat, Solid State Commun. **89**, 441 (1994).
[11] R. Caracas and X. Gonze, Phys. Rev. B **65**, 184103 (2002).
[12] R. Caracas and X. Gonze, in *Fundamental Physics of Ferroelectrics 2002*, edited by Ronald E. Cohen, AIP Conf. Proc. **626**, 303 (2002).
[13] P. Hohenberg and W. Kohn, Phys. Rev. **136**, B864 (1964).
[14] W. Kohn and L. J. Sham, Phys. Rev. **140**, A1133 (1965).
[15] X. Gonze, R. Caracas, P. Sonnet, F. Detraux, P. Ghosez, I. Noiret, and J. Schamps, in *Fundamental Physics of Ferroelectrics 2000: Aspen Center for Physics Winter Workshop*, edited by Ronald E. Cohen, AIP Conf. Proc. No. 535 (AIP Melville, NY, 2000), pp. 13–20.
[16] X. Gonze, J.-M. Beuken, R. Caracas, F. Detraux, M. Fuchs, G.-M. Rignanese, L. Sindic, M. Verstraete, G. Zerah, F. Jollet, M. Torrent, A. Roy, M. Mikami, Ph. Ghosez, J.-Y. Raty, and D. C. Allan, Comput. Mater. Sci. **25**, 478 (2002).
[17] N. Troullier and J. L. Martins, Phys. Rev. B **43**, 1993 (1991).
[18] M. Teter, Phys. Rev. B **48**, 5031 (1993).
[19] H. J. Monkhorst and J. D. Pack, Phys. Rev. B **13**, 5188 (1976).
[20] X. Gonze, Phys. Rev. B **55**, 10 337 (1997).
[21] X. Gonze and C. Lee, Phys. Rev. B **55**, 10 355 (1997).
[22] The reindexation of the experimental diffraction pattern has been done in cooperation with Dr. Joke Hadermann (EMAT center at RUCA). A report of the full quantitative analysis of the incommensurability in the rhombohedral structure is in preparation. The analysis is based on energetic considerations and on the reproduction of the Raman experimental spectra.
[23] Ph. Ghosez, E. Cockayne, U. V. Waghmare, and K. M. Rabe, Phys. Rev. B **60**, 836 (1999).
[24] I. A. Kornev and L. Bellaiche, Phys. Rev. Lett. **89**, 115502 (2002).